



# Structure and magnetic properties of cation-disordered perovskites $\text{SrLaCrSnO}_6$ and $\text{Ca}_2\text{CeCr}_2\text{TiO}_9$

Emily C. Hunter<sup>a</sup>, Peter D. Battle<sup>a,\*</sup>, Emmanuelle Suard<sup>b</sup>, Pascal Manuel<sup>c</sup>

<sup>a</sup> Inorganic Chemistry Laboratory, University of Oxford, South Parks Road, Oxford OX1 3QR, UK

<sup>b</sup> Institut Laue-Langevin, BP156, 71 avenue des Martyrs, 38000 Grenoble, France

<sup>c</sup> ISIS Facility, Rutherford Appleton Laboratory-STFC, Chilton, Didcot, Oxfordshire OX11 0QX, UK

## ARTICLE INFO

### Keywords:

Cation disorder  
Antiferromagnet  
Neutron diffraction  
Perovskite

## ABSTRACT

Polycrystalline samples of the new perovskites  $\text{SrLaCrSnO}_6$  and  $\text{Ca}_2\text{CeCr}_2\text{TiO}_9$  have been synthesised using the ceramic method and characterized by x-ray diffraction, neutron diffraction and magnetometry. Both crystallise in the space group  $Pbnm$ , with a disordered distribution of B-site cations, and both exhibit  $G_z$ -type antiferromagnetism at low temperatures. The antiferromagnetic order develops over a large temperature range. It is proposed that isolated antiferromagnetic clusters grow in size upon cooling to form a long-range antiferromagnetically-ordered backbone running through the structure. Cations with few magnetic nearest-neighbours remain decoupled from the backbone down to 2 K. More decoupled clusters are present in  $\text{Ca}_2\text{CeCr}_2\text{TiO}_9$  than in  $\text{SrLaCrSnO}_6$ . This is attributed to the increase in frustration that accompanies the increase in strength of the next-nearest-neighbour interactions that occurs when  $d^{10}:\text{Sn}^{4+}$  is replaced by  $d^0:\text{Ti}^{4+}$ .

## 1. Introduction

A simple cubic perovskite has the empirical formula  $\text{ABO}_3$  where  $A$  is normally a relatively-large divalent or trivalent cation and  $B$  is a smaller transition-metal or  $p$ -block cation. The perovskite structure has been shown to be very amenable to cation substitution at the  $A$  site, the  $B$  site or both [1,2], giving rise to a range of magnetic properties such as ferromagnetism, antiferromagnetism and ferrimagnetism. Antiferromagnetism is the most common but ferrimagnetism can occur when there is partial cation ordering over the  $B$  sites, as is the case in the triple perovskite  $\text{LaSr}_2\text{Cr}_2\text{SbO}_9$ . In this compound two crystallographically-distinct  $B$  sites are ordered in a 1:1 checkerboard arrangement [3]; 87% of the sites on one sublattice and 46% of those on the other are occupied by  $\text{Cr}$ . Hence, even though the dominant superexchange interaction between the two sites is antiferromagnetic the magnetisations of the two sublattices do not cancel, and ferrimagnetic behaviour is observed below a Curie temperature of 150 K. Ferromagnetism is relatively rare in insulating mixed-metal oxides. However, although the double perovskite  $\text{Sr}_2\text{CrSbO}_6$  is, as might be expected, an antiferromagnet,  $\text{Ca}_2\text{CrSbO}_6$  is ferromagnetic below 14 K [4,5].

We have carried out a number of syntheses in an attempt to find other compounds that behave similarly to those described above. Our attempts to prepare new ferrimagnets in which the six-coordinate sites are occupied by  $\text{Cr}^{3+}$  and a diamagnetic cation in a 2:1 ratio have led us

to  $\text{Ca}_2\text{CeCr}_2\text{TiO}_9$  and, guided by the behaviour of  $\text{Sr}_{2-x}\text{Ca}_x\text{CrSbO}_6$ , our search for new ferromagnets in which  $\text{Cr}^{3+}$  and a diamagnetic cation occupy the  $B$  sites in a 1:1 ratio has led to the synthesis of  $\text{SrLaCrSnO}_6$ . Neither of these compounds shows the type of behaviour we were seeking but they do have interesting magnetic properties and both are reminiscent of  $\text{SrLaFeSnO}_6$  [6]. The similarities between them have prompted us to present the results of our two initially-independent studies in the same paper.

## 2. Experimental

Polycrystalline samples of  $\text{Ca}_2\text{CeCr}_2\text{TiO}_9$  and  $\text{SrLaCrSnO}_6$  were synthesised using the traditional ceramic method. To form  $\text{SrLaCrSnO}_6$ , stoichiometric quantities of  $\text{SrCO}_3$ ,  $\text{Cr}_2\text{O}_3$ ,  $\text{SnO}_2$  and pre-dried  $\text{La}_2\text{O}_3$  were ground in an agate pestle and mortar for 30 min and then fired at 900 °C as a loose powder for 16 h. The resulting mixture was reground, pelletised and fired at 1300 °C for 6 h. The sample was subsequently fired at 1350 °C for 48 h and then at 1400 °C for 48 h at a time until the reaction was deemed, on the basis of the X-ray powder diffraction pattern, to have gone to completion. After each firing the sample was quench-cooled to room temperature and reground and re-pelletised. Stoichiometric quantities of  $\text{CaCO}_3$ ,  $\text{Cr}_2\text{O}_3$ ,  $\text{TiO}_2$  and pre-dried  $\text{CeO}_2$  were used as starting materials to form  $\text{Ca}_2\text{CeCr}_2\text{TiO}_9$ . The same firing sequence was used to form

\* Corresponding author.

E-mail address: [peter.battle@chem.ox.ac.uk](mailto:peter.battle@chem.ox.ac.uk) (P.D. Battle).

$\text{Ca}_2\text{CeCr}_2\text{TiO}_9$  as was used to form  $\text{SrLaCrSnO}_6$  except that an additional final firing at 1450 °C for 48 h was required. The polycrystalline sample of  $\text{SrLaCrSnO}_6$  produced was brown in colour whereas  $\text{Ca}_2\text{CeCr}_2\text{TiO}_9$  was a fine black powder.

The progress of the syntheses was monitored using X-ray powder diffraction (XRD) data collected in our laboratory on a PANalytical Empyrean diffractometer operating with  $\text{Cu K}\alpha_1$  radiation over an angular range of  $5 \leq 2\theta/^\circ \leq 125$  at room temperature. Further powder diffraction data were collected using a Si-calibrated wavelength of  $\lambda = 0.8259 \text{ \AA}$  on the instrument I11 at the RAL Diamond Light Source [7]. In the latter case, the samples were loaded into a 0.3 mm diameter borosilicate glass capillary and data were collected at room temperature using the Mythen position-sensitive detector (PSD) over an angular range of  $2 \leq 2\theta/^\circ \leq 92$ . The data were analysed using the Rietveld method [8], as implemented in the GSAS program suite [9], in order to determine the unit cell parameters. A cylindrical absorption correction for each sample was estimated using the Argonne X-ray Absorption calculator [10]. A pseudo-Voigt function [11] was employed to model the peak shapes and the background was modelled using a 20-term shifted Chebyshev function.

Neutron powder diffraction (NPD) data were collected on  $\text{SrLaCrSnO}_6$  using the instrument D2b at the ILL, Grenoble. NPD data were collected at 3.5 K, 60 K, 110 K, 200 K and at room temperature over an angular range  $0 \leq 2\theta/^\circ \leq 150$  in steps of  $\Delta 2\theta = 0.05^\circ$  using a wavelength of  $1.594 \text{ \AA}$ . The sample was loaded into a 6 mm diameter vanadium can and mounted in a displax refrigerator for all measurements below room temperature. Each dataset was fully analysed using the Rietveld method. A pseudo-Voigt function was employed to model the peak shapes and the background was modelled using a 12-term shifted Chebyshev function.

Neutron powder diffraction (NPD) data were collected on  $\text{Ca}_2\text{CeCr}_2\text{TiO}_9$  on the WISH time-of-flight diffractometer [12] at the ISIS spallation source at 1.6 K, 60 K, 110 K, 200 K and at room temperature. The sample was loaded into a 6 mm diameter cylindrical vanadium sample can and mounted in an Oxford Instruments cryostat when data were to be collected below room temperature. The data collected on banks 2–9 were refined simultaneously using the Rietveld method. A pseudo-Voigt function was employed to model the peak shapes and the background was modelled using a 12-term shifted Chebyshev function for banks 2/9 and 3/8 and a 20-term shifted Chebyshev function for banks 4/7 and 5/6. The scattering angles for the different detector banks are as follows: banks 2/9,  $58^\circ$ ; banks 3/8,  $90^\circ$ ; banks 4/7,  $122^\circ$  and banks 5/6,  $153^\circ$ .

DC magnetometry data were collected on both compounds using a Quantum Design SQUID magnetometer. The measurements were taken on warming the samples through the temperature range  $2 \leq T/\text{K} \leq 300$  in a field of 100 Oe, firstly after cooling from room temperature to 2 K in zero field (ZFC) and subsequently after cooling in the measuring field (FC). The magnetisation per formula unit (f. u.) of the samples was also measured as a function of applied field at 5, 60, 110 and 200 K for  $\text{SrLaCrSnO}_6$  and at 5, 100 and 200 K for  $\text{Ca}_2\text{CeCr}_2\text{TiO}_9$  over a field range of  $-50 \leq H/\text{kOe} \leq 50$ .

### 3. Results

Our XRD data showed that both  $\text{SrLaCrSnO}_6$  and  $\text{Ca}_2\text{CeCr}_2\text{TiO}_9$  crystallise in the space group  $Pbnm$ . The 4e site is occupied by a disordered arrangement of either 1:1 Sr/La or 2:1 Ca/Ce, and the 4d site by a disordered arrangement of either a 1:1 Cr/Sn or 2:1 Cr/Ti. Two crystallographically-distinct oxide ions occupy 4e and 8f sites. The Rietveld fits to the data collected on I11 are shown in Fig. 1;  $R_{\text{wp}} = 0.0162$  for  $\text{SrLaCrSnO}_6$  and  $R_{\text{wp}} = 0.0365$  for  $\text{Ca}_2\text{CeCr}_2\text{TiO}_9$ .  $\text{SrLaCrSnO}_6$  was found to be contaminated with 0.44(2) wt%  $\text{La}_2\text{Sn}_2\text{O}_7$  and  $\text{Ca}_2\text{CeCr}_2\text{TiO}_9$  with 3.77(3) wt%  $\text{CaTiO}_3$  and 0.1(1) wt%  $\text{CeO}_2$ .

The temperature dependence of the molar magnetic susceptibility,  $\chi(T)$ , of  $\text{SrLaCrSnO}_6$  is shown in Fig. 2. There is a slight divergence of

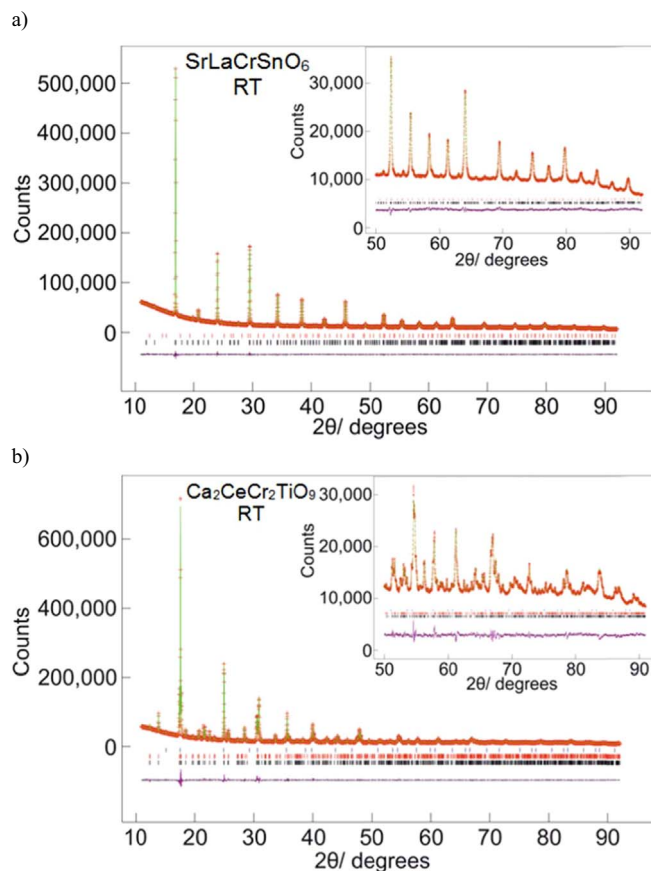


**Fig. 1.** Observed (red crosses) and calculated (green line) synchrotron x-ray diffraction profiles of a)  $\text{SrLaCrSnO}_6$  and b)  $\text{Ca}_2\text{CeCr}_2\text{TiO}_9$  collected at room temperature on I11 and fitted using the space group  $Pbnm$ . Reflection markers are shown top to bottom for a)  $\text{La}_2\text{Sn}_2\text{O}_7$  (red) and  $\text{SrLaCrSnO}_6$  (black) and b)  $\text{CeO}_2$  (blue),  $\text{CaTiO}_3$  (red) and  $\text{Ca}_2\text{CeCr}_2\text{TiO}_9$  (black). (For interpretation of the references to color in this figure legend, the reader is referred to the web version of this article)

the ZFC and FC curves below 200 K, which is most noticeable in the plot of the inverse molar susceptibility against temperature shown in the inset. This divergence becomes more marked below 150 K. The ZFC susceptibility levels out at 80 K and there is a clear change in the gradient of both the ZFC and FC inverse susceptibilities at this temperature. Below 35 K there appears to be a paramagnetic-like upturn that becomes more prominent below 12 K. From a Curie-Weiss fit to the inverse susceptibility in the temperature range  $200 \leq T/\text{K} \leq 300$ , the effective magnetic moment per  $\text{Cr}^{3+}$  cation was found to be  $4.25(13) \mu_B$  and the Weiss temperature was found to be  $-360(3) \text{ K}$ . The field dependence of the magnetisation per formula unit at 5, 60, 110 and 200 K is shown in Fig. 3.  $M(H)$  is linear at 200 K and at 110 K but at 60 K there is a small amount of magnetic hysteresis and a slight non-linearity to the curve, which is more pronounced at 5 K. The magnetisation does not saturate and is only  $0.14 \mu_B$  per formula unit at 5 K and 50 kOe.

The temperature dependence of the molar magnetic susceptibility of  $\text{Ca}_2\text{CeCr}_2\text{TiO}_9$ , shown in Fig. 4, shows similar behaviour to that of  $\text{SrLaCrSnO}_6$  except that the transitions are sharper and larger in magnitude. The ZFC and FC susceptibilities differ below 175 K; this is again more obvious in  $\chi^{-1}(T)$ . A Curie-Weiss fit in the region  $200 \leq T/\text{K} \leq 300$  gave an effective magnetic moment per  $\text{Cr}^{3+}$  cation of  $4.53(13) \mu_B$  and a Weiss temperature of  $-466(2) \text{ K}$ . At 80 K there is a sharp change in gradient in both the ZFC and FC susceptibilities, with both increasing in magnitude on cooling. At 2 K this increase is tending towards a plateau of  $1.44 \text{ cm}^3 \text{ mol}^{-1}$  for the FC curve and  $0.36 \text{ cm}^3 \text{ mol}^{-1}$  for the ZFC curve. Fig. 5 shows that  $M(H)$  is linear at 200 K but a small amount of hysteresis is present at 100 K and an increased level is

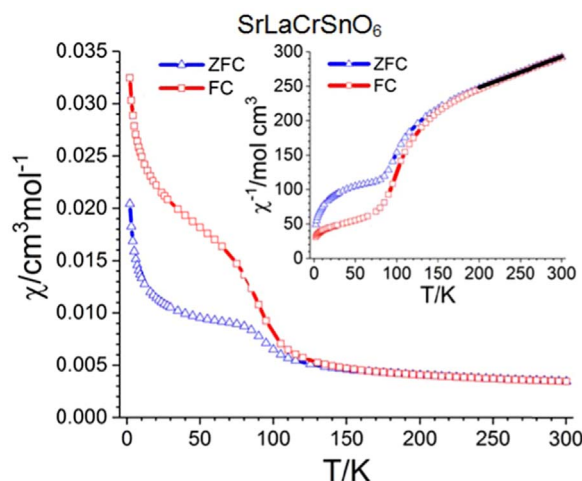


**Fig. 2.** The ZFC and FC molar dc susceptibility of  $\text{SrLaCrSnO}_6$  measured in an applied field of 100 Oe as a function of temperature.

clearly present at 2 K. At 2 K the magnetisation does not saturate but has a coercive field of 2.45 kOe and a remanent magnetisation of  $\sim 0.034 \mu_B$  per formula unit.

Rietveld analysis of the NPD patterns collected at room temperature confirmed that both compounds crystallise in the space group  $Pbnm$ . In view of the relatively high level of  $\text{CaTiO}_3$  detected at the synchrotron X-ray source, the occupancies of the cation sites in  $\text{Ca}_2\text{CeCr}_2\text{TiO}_9$  were allowed to vary during our analysis of the NPD data collected at room temperature. Constraints were applied to ensure that both the A and B sites remained fully occupied and that  $\text{Ca}^{2+}$  and  $\text{Ti}^{4+}$  cations left the structure in equal numbers, whilst rescaling the composition to leave no vacancies on the oxygen sites. This strategy gave a refined composition of  $\text{Ca}_{1.969}\text{Ce}_{1.031}\text{Cr}_{2.062}\text{Ti}_{0.938}\text{O}_9$ , corresponding to an impurity concentration of 2.64 wt%, which was used subsequently during the analysis of the diffraction data collected at lower temperatures. Note that for simplicity we shall continue to use the ideal formula in our text. The fits to the diffraction patterns recorded from both compounds at room temperature are shown in Fig. 6. The corresponding structural parameters and selected bond lengths and angles are listed in Table 1–6. No cation ordering was detected in either compound when test refinements were carried out in the monoclinic space group  $P2_1/n$ .

The NPD pattern collected from  $\text{SrLaCrSnO}_6$  at 200 K could be accounted for using the same structural model that was used in the

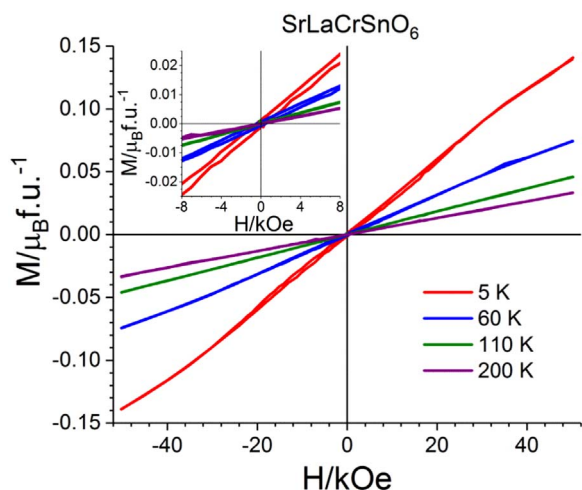


**Fig. 3.** The magnetisation per formula unit of  $\text{SrLaCrSnO}_6$  as a function of magnetic field at 5 K, 60 K, 110 K and 200 K.

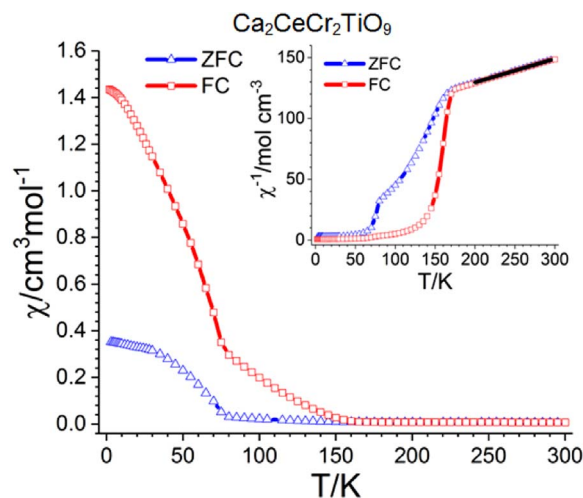


**Fig. 4.** The ZFC and FC molar dc susceptibility of  $\text{Ca}_2\text{CeCr}_2\text{TiO}_9$  measured in an applied field of 100 Oe as a function of temperature.

analysis of the data collected at room temperature. On cooling to 110 K a small amount of diffuse scattering at the position of the (101)/(011) reflection is visible, see Fig. 7, but it was not included in our quantitative analysis of the pattern. By 60 K it had developed into a Bragg reflection which grew in intensity on cooling to 3.5 K. This reflection can be accounted for by the inclusion in the model of a  $G_z$  magnetic structure [13] involving the  $\text{Cr}^{3+}$  cations on the B site, see Fig. 8. The ordered magnetic moment per  $\text{Cr}^{3+}$  cation,  $M_O$ , refined to be  $1.63(4) \mu_B$  and  $2.24(3) \mu_B$  at 60 K and 3.5 K, respectively. The atomic coordinates, bond lengths and bond angles determined in these analyses are included in Tables 1–3.

Similarly, no magnetic Bragg scattering is apparent in the diffraction pattern collected at 200 K from  $\text{Ca}_2\text{CeCr}_2\text{TiO}_9$  but Bragg peaks corresponding to the (101)/(011) reflection of a  $G_z$  magnetic structure appear at  $d \sim 4.4 \text{ \AA}$  on cooling, see Fig. 9 and Figs. S1–S5. The peak is first visible in the data collected at 110 K and grows in intensity on cooling to 60 K and 1.6 K. The increase in intensity is reflected in the refined ordered moments of the  $\text{Cr(III)}$  cation; at 110 K  $M_O = 0.89(1) \mu_B$ , at 60 K  $M_O = 1.490(5) \mu_B$  and at 1.6 K  $M_O = 1.974(5) \mu_B$ . The atomic coordinates, bond lengths and bond angles determined in these analyses are included in Tables 4–6.

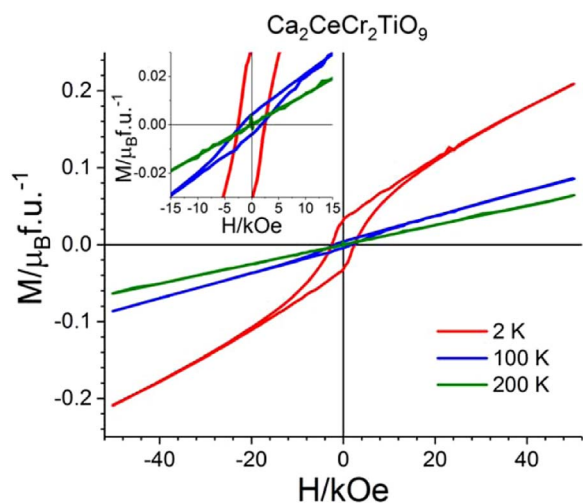


**Fig. 5.** The magnetisation per formula unit of  $\text{Ca}_2\text{CeCr}_2\text{TiO}_9$  as a function of magnetic field at 2 K, 100 K and 200 K.

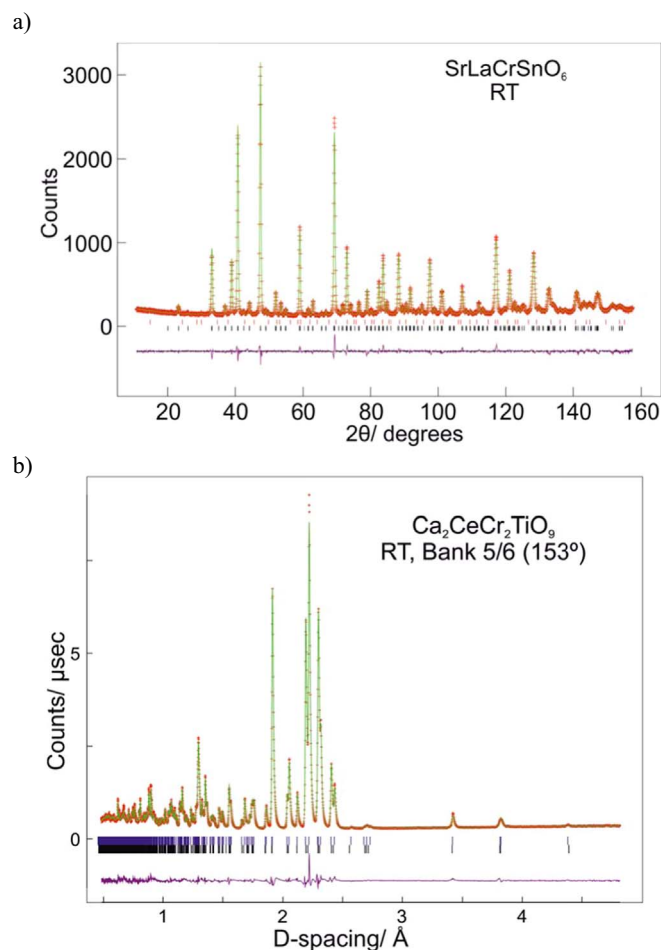


**Fig. 6.** Observed (red crosses) and calculated (green line) neutron powder diffraction profiles of a)  $\text{SrLaCrSnO}_6$  and b)  $\text{Ca}_2\text{CeCr}_2\text{TiO}_9$  at room temperature. Reflection markers are shown top to bottom for a)  $\text{La}_2\text{Sn}_2\text{O}_7$  (red) and  $\text{SrLaCrSnO}_6$  (black) and b)  $\text{Ca}_2\text{CeCr}_2\text{TiO}_9$  (blue), and  $\text{CaTiO}_3$  (black). (For interpretation of the references to color in this figure legend, the reader is referred to the web version of this article)

**Table 1**  
Structural parameters of  $\text{SrLaCrSnO}_6$  at 300 K, 200 K, 110 K, 60 K and 3.5 K.

		300 K	200 K	110 K	60 K	3.5 K
$a/\text{\AA}$		5.61732(14)	5.61156(12)	5.60834(11)	5.60736(12)	5.60709(13)
$b/\text{\AA}$		5.60122(12)	5.59658(11)	5.59447(10)	5.59388(11)	5.59383(11)
$c/\text{\AA}$		7.92122(18)	7.91399(16)	7.91072(15)	7.90958(16)	7.90947(16)
$V/\text{\AA}^3$		249.232(10)	248.544(9)	248.204(8)	248.099(9)	248.082(9)
$R_{\text{wp}}$		0.0399	0.0397	0.0390	0.0415	0.0417
Sr/La	$x$	−0.0020(5)	−0.0016(5)	−0.0020(4)	−0.0019(5)	−0.0018(5)
	$y$	0.01802(26)	0.01931(24)	0.02054(22)	0.02113(23)	0.02092(23)
	$z$	$1/4$	$1/4$	$1/4$	$1/4$	$1/4$
	$U_{\text{iso}}/\text{\AA}^2$	0.01276(22)	0.01143(22)	0.01012(21)	0.00899(22)	0.00887(22)
Cr/Sn	Sr Occupancy	$1/2$	$1/2$	$1/2$	$1/2$	$1/2$
	La Occupancy	$1/2$	$1/2$	$1/2$	$1/2$	$1/2$
	$U_{\text{iso}}/\text{\AA}^2$	0.00124(22)	0.00103(22)	0.00077(21)	0.00060(23)	0.00046(23)
	Cr Occupancy	$1/2$	$1/2$	$1/2$	$1/2$	$1/2$
4d (0 $1/2$ 0)	Sn Occupancy	$1/2$	$1/2$	$1/2$	$1/2$	$1/2$
	$x$	0.06499(35)	0.06527(34)	0.06620(33)	0.06641(35)	0.06668(36)
	$y$	0.49284(41)	0.49254(38)	0.49196(36)	0.49143(38)	0.49150(38)
	$z$	$1/4$	$1/4$	$1/4$	$1/4$	$1/4$
O1	$U_{\text{iso}}/\text{\AA}^2$	0.00958(38)	0.00788(37)	0.00788(35)	0.00677(37)	0.00688(37)
	$x$	0.72485(22)	0.72382(22)	0.72331(20)	0.72290(22)	0.72293(22)
	$y$	0.27505(23)	0.27556(24)	0.27573(22)	0.27622(25)	0.27643(25)
	$z$	0.03271(16)	0.03352(15)	0.03396(14)	0.03394(15)	0.03396(15)
O2	$U_{\text{iso}}/\text{\AA}^2$	0.00981(28)	0.00858(27)	0.00718(26)	0.00668(27)	0.00638(27)

**Table 2**

Bond lengths ( $\text{\AA}$ ) in  $\text{SrLaCrSnO}_6$  at 300 K, 200 K, 110 K, 60 K and 3.5 K.

	300 K	200 K	110 K	60 K	3.5 K
Sr/La–O1	2.459(3)	2.453(3)	2.449(3)	2.447(3)	2.445(3)
Sr/La–O1	2.686(3)	2.675(2)	2.665(2)	2.659(2)	2.660(2)
Sr/La–O1	2.966(3)	2.972(2)	2.982(2)	2.988(2)	2.986(2)
Sr/La–O1	3.166(3)	3.167(3)	3.168(3)	3.170(3)	3.172(3)
Sr/La–O2	2.526(2)	2.520(2)	2.5175(18)	2.517(2)	2.515(2)
Sr/La–O2	2.526(2)	2.520(2)	2.5175(18)	2.517(2)	2.515(2)
Sr/La–O2	2.718(2)	2.7142(19)	2.7079(17)	2.709(2)	2.710(2)
Sr/La–O2	2.718(2)	2.7142(19)	2.7079(17)	2.709(2)	2.710(2)
Sr/La–O2	2.8252(18)	2.8199(17)	2.8180(16)	2.8138(17)	2.8138(17)
Sr/La–O2	2.8252(18)	2.8199(17)	2.8180(16)	2.8138(17)	2.8138(17)
Sr/La–O2	3.1833(17)	3.1917(16)	3.1993(15)	3.2028(17)	3.2025(17)
Sr/La–O2	3.1833(17)	3.1917(16)	3.1993(15)	3.2028(17)	3.2025(17)
< Sr/La–O >	2.815	2.813	2.812	2.812	2.812
Cr/Sn–O1	2.0141(4)	2.0126(4)	2.0127(3)	2.0127(4)	2.0130(4)
Cr/Sn–O2	2.0090(14)	2.0066(14)	2.0050(13)	2.0055(15)	2.0064(14)
Cr/Sn–O2'	2.0109(14)	2.0125(14)	2.0136(13)	2.0133(15)	2.0124(15)
< Cr/Sn–O >	2.011	2.011	2.010	2.011	2.011

**Table 3**

Bond angles (deg) in  $\text{SrLaCrSnO}_6$  at 300 K, 200 K, 110 K, 60 K and 3.5 K.

	300 K	200 K	110 K	60 K	3.5 K
O1–Cr/Sn–O2	90.01(8)	90.01(8)	90.04(7)	90.12(8)	90.14(8)
O1–Cr/Sn–O2	90.14(8)	90.14(8)	90.16(7)	90.17(8)	90.14(8)
O2–Cr/Sn–O2	91.108(12)	91.132(12)	91.138(11)	91.134(12)	91.139(12)
< O–Cr/Sn–O >	90.42	90.43	90.45	90.47	90.47
Cr/Sn–O1–Cr/Sn	158.99(11)	158.89(11)	158.58(10)	158.50(11)	158.42(11)
Cr/Sn–O2–Cr/Sn	161.29(6)	160.79(6)	160.54(6)	160.43(6)	160.40(6)
< Cr/Sn–O–Cr/Sn >	160.14	159.84	159.56	159.47	159.41



**Table 4**Structural parameters of  $\text{Ca}_2\text{CeCr}_2\text{TiO}_9$  at 300 K, 200 K, 110 K, 60 K and 1.6 K.

		300 K	200 K	110 K	60 K	1.6 K
$a/\text{\AA}$		5.35343(16)	5.34826(15)	5.34480(15)	5.34430(14)	5.34389(14)
$b/\text{\AA}$		5.45709(15)	5.45692(16)	5.45636(16)	5.45618(15)	5.45580(14)
$c/\text{\AA}$		7.62924(23)	7.62355(22)	7.61940(22)	7.61871(22)	7.61820(21)
$V/\text{\AA}^3$		222.882(11)	222.494(11)	222.206(11)	222.158(11)	222.110(10)
$R_{\text{wp}}$		0.0396	0.0377	0.0380	0.0386	
Ca/Ce	$x$	−0.01058(17)	−0.01068(16)	−0.01052(16)	−0.01052(16)	−0.01044(17)
4e	$y$	0.04265(12)	0.04416(12)	0.04498(12)	0.04522(12)	0.04521(12)
	$z$	$\frac{1}{4}$	$\frac{1}{4}$	$\frac{1}{4}$	$\frac{1}{4}$	$\frac{1}{4}$
	$U_{\text{iso}}/\text{\AA}^2$	0.01685(22)	0.01393(21)	0.01312(21)	0.01255(21)	0.01230(22)
	Ca Occupancy	0.656(1)	0.656(1)	0.656(1)	0.656(1)	0.656(1)
	Ce Occupancy	0.344(1)	0.344(1)	0.344(1)	0.344(1)	0.344(1)
Cr/Ti	$U_{\text{iso}}/\text{\AA}^2$	0.0075(11)	0.0029(6)	0.0026(6)	0.0023(6)	0.0014(6)
4d (0 $\frac{1}{2}$ 0)	Cr Occupancy	0.687(1)	0.687(1)	0.687(1)	0.687(1)	0.687(1)
	Ti Occupancy	0.313(1)	0.313(1)	0.313(1)	0.313(1)	0.313(1)
O1	$x$	0.08711(13)	0.08707(13)	0.08726(13)	0.08729(13)	0.08705(13)
4e	$y$	0.47564(10)	0.47527(9)	0.47507(9)	0.47494(9)	0.47490(10)
	$z$	$\frac{1}{4}$	$\frac{1}{4}$	$\frac{1}{4}$	$\frac{1}{4}$	$\frac{1}{4}$
	$U_{\text{iso}}/\text{\AA}^2$	0.01462(21)	0.01165(20)	0.01124(20)	0.01114(20)	0.01106(20)
O2	$x$	0.70395(7)	0.70362(7)	0.70345(7)	0.70343(7)	0.70333(7)
8f	$y$	0.29491(6)	0.29519(6)	0.29526(6)	0.29526(6)	0.29532(6)
	$z$	0.04360(6)	0.04422(6)	0.04441(6)	0.04439(6)	0.04435(6)
	$U_{\text{iso}}/\text{\AA}^2$	0.01453(18)	0.01189(17)	0.01150(17)	0.01137(17)	0.00647(26)

**Table 5**Bond lengths ( $\text{\AA}$ ) in  $\text{Ca}_2\text{CeCr}_2\text{TiO}_9$  at 300 K, 200 K, 110 K, 60 K and 1.6 K.

	300 K	200 K	110 K	60 K	1.6 K
Ca/Ce–O1	2.2963(12)	2.2965(11)	2.2942(12)	2.2942(12)	2.2948(12)
Ca/Ce–O1	2.4200(7)	2.4099(7)	2.4042(7)	2.4022(7)	2.4015(7)
Ca/Ce–O1	3.1080(12)	3.1055(12)	3.1061(12)	3.1062(12)	3.1051(12)
Ca/Ce–O1	3.1381(8)	3.1481(7)	3.1533(7)	3.1552(7)	3.1548(8)
Ca/Ce–O2	2.3192(7)	2.3177(7)	2.3182(7)	2.3188(7)	2.3186(8)
Ca/Ce–O2	2.3192(7)	2.3177(7)	2.3182(7)	2.3188(7)	2.3186(8)
Ca/Ce–O2	2.5904(7)	2.5831(7)	2.5799(7)	2.5791(8)	2.5800(8)
Ca/Ce–O2	2.5904(7)	2.5831(7)	2.5799(7)	2.5791(8)	2.5800(8)
Ca/Ce–O2	2.6688(6)	2.6670(6)	2.6645(6)	2.6637(6)	2.6628(6)
Ca/Ce–O2	2.6688(6)	2.6670(6)	2.6645(6)	2.6637(6)	2.6628(6)
< Ca/Ce–O >	2.612	2.610	2.608	2.608	2.608
Cr/Ti–O1	1.9680(2)	1.9666(2)	1.9658(2)	1.9657(2)	1.9653(2)
Cr/Ti–O2	1.9685(3)	1.9686(3)	1.9684(3)	1.9683(3)	1.9684(3)
Cr/Ti–O2'	1.9730(3)	1.9734(3)	1.9729(3)	1.9727(3)	1.9725(4)
< Cr/Ti–O >	1.970	1.970	1.969	1.969	1.969

#### 4. Discussion

The structural chemistry of  $\text{SrLaCrSnO}_6$  is very similar to that of  $\text{Ca}_2\text{CeCr}_2\text{TiO}_9$ . They both crystallise in the orthorhombic space group  $Pbnm$  and hence show no cation ordering over the six-coordinate sites. The average bond lengths are as expected; < Ca/Ce–O > is significantly shorter than < Sr/La–O >, which is consistent with  $\text{Ce}^{4+}$  and  $\text{Ca}^{2+}$  both being smaller than  $\text{La}^{3+}$  and  $\text{Sr}^{2+}$ , and < Cr/Ti–O > is significantly shorter than < Cr/Sn–O >, again consistent with the difference in ionic radius of the tetravalent cations [14]. The degree of octahedral tilting in  $\text{Ca}_2\text{CeCr}_2\text{TiO}_9$  is sizable; the average tilt angle is  $\sim 14^\circ$ , which is

comparable to the degree of tilting in  $\text{Ca}_2\text{CrSbO}_6$  [5]. However,  $\text{SrLaCrSnO}_6$  has an average tilt angle of only  $\sim 10^\circ$ . There is a slight reduction in the unit cell volume upon cooling both samples but there is remarkably little change in the average bond lengths and angles. No change in space group symmetry was observed.

Fitting  $\chi^{-1}(T)$  to the Curie-Weiss law resulted in a large negative Weiss temperature and an effective moment per  $\text{Cr}^{3+}$  ion that is much greater than the theoretical value of  $3.87 \mu_B$  for both  $\text{SrLaCrSnO}_6$  and  $\text{Ca}_2\text{CeCr}_2\text{TiO}_9$ . Given that  $\text{LaCrO}_3$  orders antiferromagnetically at 290 K [15], it is likely that significant short-range magnetic ordering is present in the temperature range  $200 < T/K < 300$ , thus rendering the parameters derived from the Curie-Weiss law in that temperature range physically meaningless. The observation of a difference between the ZFC and FC  $\chi(T)$  curves at temperatures as high as 200 and 175 K in  $\text{SrLaCrSnO}_6$  and  $\text{Ca}_2\text{CeCr}_2\text{TiO}_9$ , respectively, is consistent with this explanation. The behaviour of both curves below 200 K is unusual and will be discussed below.

Our neutron diffraction data indicate that, in contrast to  $\text{Ca}_2\text{CrSbO}_6$  and  $\text{LaSr}_2\text{Cr}_2\text{SbO}_9$ , respectively,  $\text{SrLaCrSnO}_6$  and  $\text{Ca}_2\text{CeCr}_2\text{TiO}_9$  both adopt a G-type antiferromagnetic ground state with no net magnetisation in the absence of an applied field. In the case of  $\text{Ca}_2\text{CeCr}_2\text{TiO}_9$  this is clearly attributable to the absence of the B-site cation ordering that is directly responsible for the ferrimagnetism of  $\text{LaSr}_2\text{Cr}_2\text{SbO}_9$ . The ferromagnetism of  $\text{Ca}_2\text{CrSbO}_6$  has been attributed to the high tilt angle of the  $\text{CrO}_6$  octahedra therein. A similar level of tilting is present in  $\text{SrLaCrSnO}_6$  but the absence of cation ordering leads to the presence of strong nearest-neighbour antiferromagnetic Cr–O–Cr superexchange interactions that are absent from the cation-ordered antimonate and so, once again, the change in magnetic behaviour can be traced to the absence of cation ordering. The loss of cation ordering is a consequence

**Table 6**Bond angles (deg) in  $\text{Ca}_2\text{CeCr}_2\text{TiO}_9$  at 300 K, 200 K, 110 K, 60 K and 1.6 K.

	300 K	200 K	110 K	60 K	1.6 K
O1–Cr/Ti–O2	91.308(24)	91.211(24)	91.208(24)	91.231(24)	91.222(25)
O1–Cr/Ti–O2	90.654(27)	90.815(26)	90.848(26)	90.851(27)	90.872(28)
O2–Cr/Ti–O2	90.589(6)	90.583(6)	90.564(6)	90.559(6)	90.554(6)
< O–Cr/Ti–O >	90.85	90.87	90.87	90.88	90.88
Cr/Ti–O1–Cr/Ti	151.47(4)	151.45(4)	151.38(4)	151.36(4)	151.43(4)
Cr/Ti–O2–Cr/Ti	151.738(23)	151.464(23)	151.374(23)	151.377(24)	151.364(24)
< Cr/Ti–O–Cr/Ti >	151.60	151.46	151.38	151.37	151.40

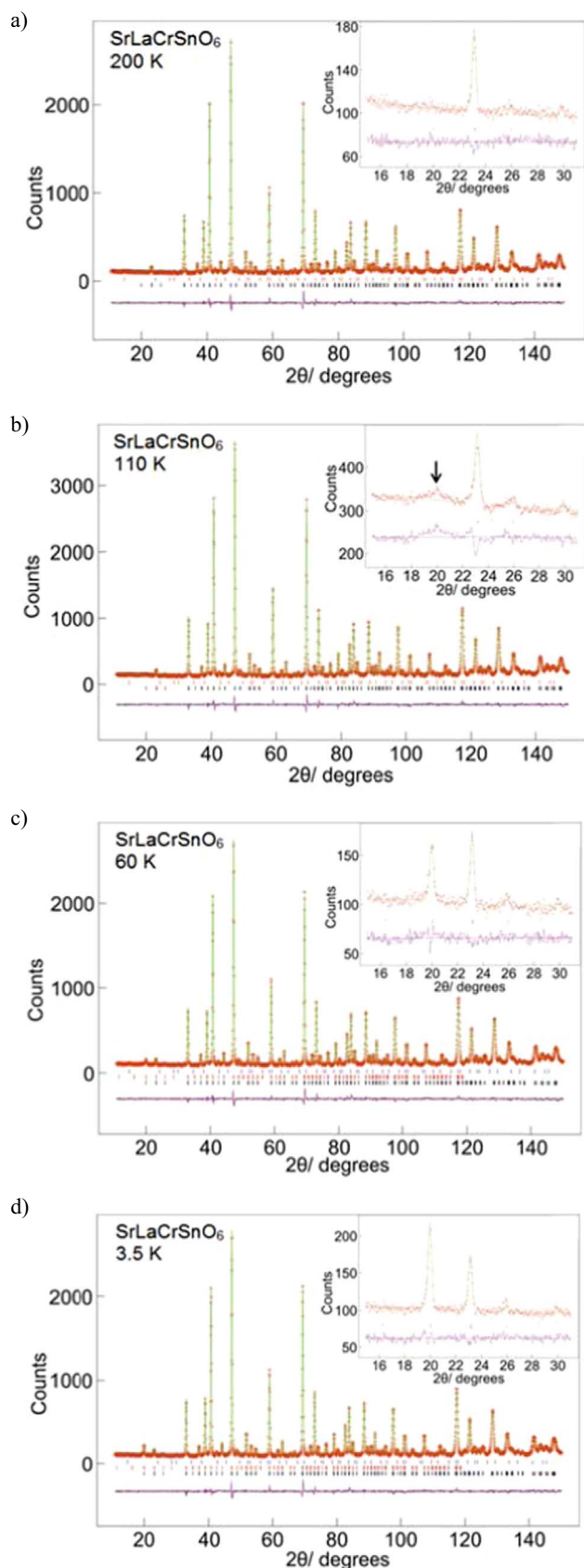


**Fig. 7.** Observed (red crosses) and calculated (green line) neutron powder diffraction profiles of  $\text{SrLaCrSnO}_6$  collected at room a) 200 K, b) 110 K, c) 60 K and d) 3.5 K. Reflection markers are shown top to bottom in a) and b) for  $\text{La}_2\text{Sn}_2\text{O}_7$  (red) and  $\text{SrLaCrSnO}_6$  (black) and in c) and d) for  $\text{La}_2\text{Sn}_2\text{O}_7$  (blue), magnetic  $\text{SrLaCrSnO}_6$  (red) and structural  $\text{SrLaCrSnO}_6$  (black). An enlarged view of the low angle region is shown in the inset. In b) the diffuse scattering peak at  $2\theta = 20.03^\circ$  is marked with an arrow. (For interpretation of the references to color in this figure legend, the reader is referred to the web version of this article)

of the small charge difference between  $\text{Cr}^{3+}$  and either  $\text{Sn}^{4+}$  or  $\text{Ti}^{4+}$ . However, the temperature dependence of the magnetic susceptibilities of these compounds is not characteristic of simple antiferromagnets. Furthermore, the ordered magnetic moment per  $\text{Cr}^{3+}$  cation is unusually low in both  $\text{SrLaCrSnO}_6$  and  $\text{Ca}_2\text{CeCr}_2\text{TiO}_9$ , and particularly so in the latter. In order to understand these results it is useful to compare the magnetic behaviour of  $\text{SrLaCrSnO}_6$  below 200 K with that of the iron analogue,  $\text{SrLaFeSnO}_6$ , which also crystallises in the space group  $Pbnm$  [6]. The ZFC and FC susceptibilities of  $\text{SrLaFeSnO}_6$  do not overlie below 250 K; the ZFC curve reaches a maximum at 38 K, suggesting the onset of antiferromagnetic ordering, while the FC curve reaches a constant value at around the same temperature. Neutron diffraction data collected at 1.7 K revealed a  $G_z$  antiferromagnetic spin arrangement at that temperature. Mössbauer spectroscopy showed that magnetic hyperfine interactions were present in  $\text{SrLaFeSnO}_6$  below 215 K, leading Attfield et al. to postulate that short-range magnetic interactions start to develop below 250 K and that long-range antiferromagnetic ordering occurs at 38 K. Gibb expanded on this model by envisaging clusters of antiferromagnetically coupled spins gradually increasing in size and linking together as the temperature is lowered until long-range order occurs along a magnetic ‘backbone’ [16]. Simulations showed that while 87% of Fe atoms in a fully disordered structure are expected to be biconnected to the magnetic backbone of the lattice, only 63% are connected by more than two nearest-neighbour pathways. Clusters with few connections to the backbone are more susceptible to competing superexchange interactions and will be the first to decouple from the magnetic backbone as the temperature is raised. They are likely to carry a small net moment due to the incomplete cancellation of spins and they will therefore enhance the susceptibility and be strongly influenced by an external magnetic field, hence the observed hysteresis in the magnetic susceptibility. The

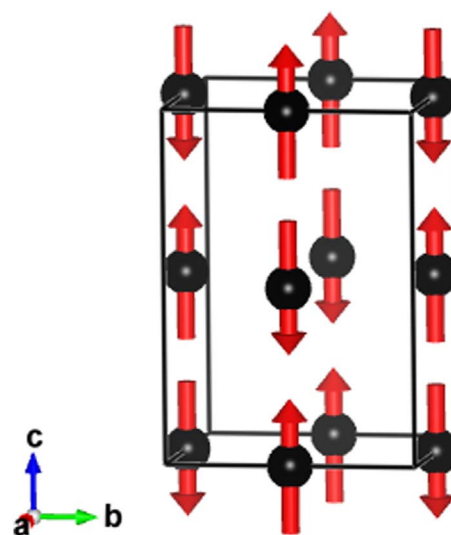


**Fig. 8.** The  $G_z$  magnetic structure adopted by  $\text{SrLaCrSnO}_6$  and  $\text{Ca}_2\text{CeCr}_2\text{TiO}_9$ . The black circles represent the B site cations and the red arrows show the orientation of the magnetic moments [21]. For clarity the A site cations and oxygen anions are omitted. (For interpretation of the references to color in this figure legend, the reader is referred to the web version of this article)

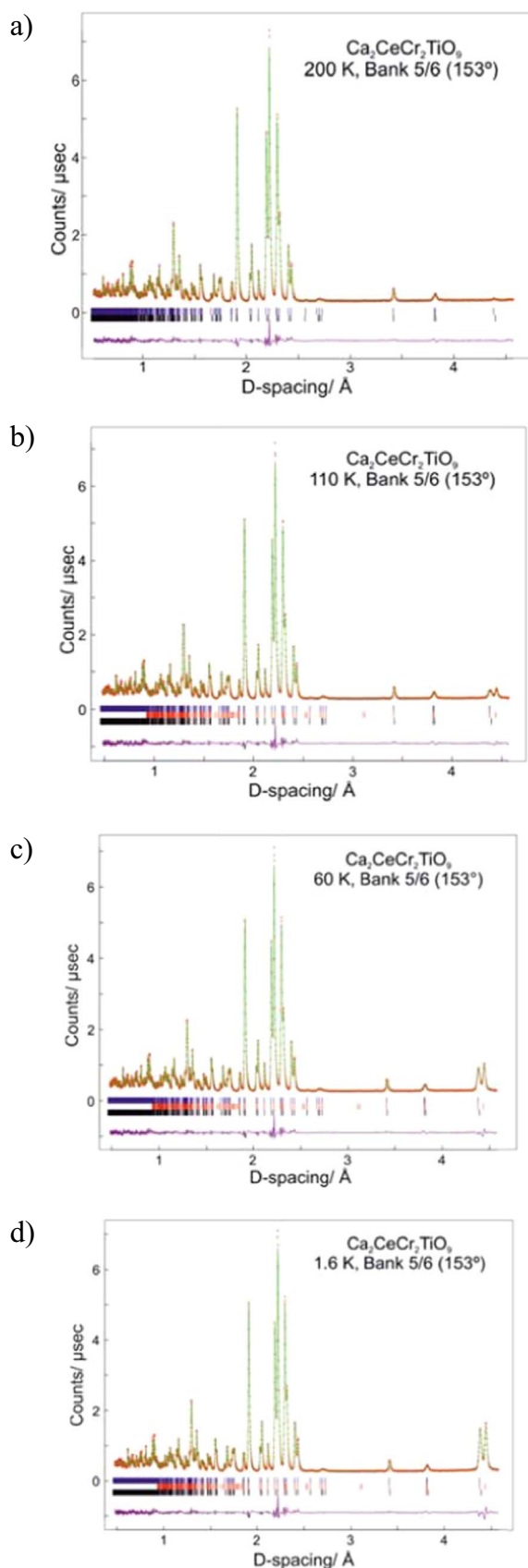


**Fig. 9.** Observed (red crosses) and calculated (green line) neutron powder diffraction profiles of  $\text{Ca}_2\text{CeCr}_2\text{TiO}_9$  collected at a) 200 K, b) 110 K, c) 60 K and d) 1.6 K. Reflection markers are shown top to bottom for  $\text{Ca}_2\text{CeCr}_2\text{TiO}_9$  (blue), magnetic  $\text{Ca}_2\text{CeCr}_2\text{TiO}_9$  (red) and  $\text{CaTiO}_3$  (black). (For interpretation of the references to color in this figure legend, the reader is referred to the web version of this article)

ordered magnetic moment per  $\text{Fe}^{3+}$  cation at 1.5 K,  $2.94 \mu_B$  [6], is very low, suggesting that even at this temperature not all of the spins and clusters are linked to the magnetic backbone.

Attfield et al. only collected neutron diffraction data on  $\text{SrLaFeSnO}_6$  at room temperature and 1.7 K but we have been able to collect data on  $\text{SrLaCrSnO}_6$  over a greater range of temperatures and hence to follow the temperature evolution of the long-range magnetic ordering. At 110 K, well below the temperature at which the ZFC and FC curves cease to overlap, no sharp magnetic Bragg peaks have developed but we do observe a broad, weak, diffuse magnetic peak showing that significant short-range antiferromagnetic interactions are present. We suggest that the decrease in gradient of  $\chi(T)$  at 80 K marks the onset of truly long-range antiferromagnetic ordering and the formation of a backbone of ordered spins. This type of ordering is certainly present at 60 K, as is shown by the presence of a sharp magnetic Bragg peak in the diffraction pattern, see Fig. 7(c). As the temperature decreases further the intensity of the magnetic Bragg scattering, representing the magnitude of the ordered moment, increases as more spin clusters join the magnetic backbone of the lattice and partake in the long-range magnetic order. The refined ordered moment per Cr ion at 3.5 K of  $2.24(3) \mu_B$  is only slightly smaller than expected given that the ordered moment per  $\text{Cr}^{3+}$  ion in  $\text{LaCrO}_3$  is  $2.63(3) \mu_B$  [17] and  $2.56(3) \mu_B$  in  $\text{Ca}_2\text{CrSbO}_6$  [5]. If we assume that only  $\text{Cr}^{3+}$  ions that are at least biconnected to the magnetic backbone (~87%) contribute to the long-range magnetic order at this temperature then the moment per  $\text{Cr}^{3+}$  ion becomes a more reasonable  $2.57 \mu_B$ . The rise in the susceptibility at the lowest temperatures measured can be attributed to the presence of the disconnected spins.

The similarity of the magnetic susceptibility and NPD data collected on  $\text{Ca}_2\text{CeCr}_2\text{TiO}_9$  to those from  $\text{SrLaFeSnO}_6$  suggests that the magnetic cluster model can also be applied to this system. The ZFC and FC  $\chi^{-1}(T)$  curves differ below 175 K, see Fig. 4, and a magnetic Bragg peak is apparent in the NPD data collected at 110 K. The refined value of the ordered moment,  $0.89(1) \mu_B$ , is, however, very small. Below the increase in gradient of  $\chi(T)$  at 80 K the intensity of the magnetic scattering increases but the ordered moment per  $\text{Cr}^{3+}$  cation at 1.6 K,  $1.974(5) \mu_B$ , is smaller than that found in  $\text{SrLaCrSnO}_6$ . This suggests that at base temperature cluster formation is extensive but that fewer spins are connected to the magnetic backbone in  $\text{Ca}_2\text{CeCr}_2\text{TiO}_9$  than in  $\text{SrLaCrSnO}_6$ . This is consistent with the larger molar susceptibility at 2 K, the larger hysteresis in  $M(H)$  and the greater difference between the ZFC and FC  $\chi(T)$  of  $\text{Ca}_2\text{CeCr}_2\text{TiO}_9$  compared to  $\text{SrLaCrSnO}_6$ . However, the B sites in  $\text{Ca}_2\text{CeCr}_2\text{TiO}_9$  contain a greater proportion of paramagnetic ions than in  $\text{SrLaCrSnO}_6$  so more ions will be at least biconnected to the magnetic backbone of the lattice. This would be expected to result in fewer clusters being decoupled from the magnetic backbone at low temperature.

The origin of this apparent contradiction may lie in the differences between the electronic structures of  $d^{10}:\text{Sn}^{4+}$  and  $d^0:\text{Ti}^{4+}$ ; the filled  $d$  orbitals of a  $p$ -block cation lie too low in energy to be involved in superexchange whereas the empty orbitals of the  $d^0$  cation are able to hybridise with the  $p$  orbitals of the  $\text{O}^{2-}$  cation and hence can play a role in the magnetic coupling [18]. Like  $\text{SrLaCrSnO}_6$  and  $\text{SrLaFeSnO}_6$ ,  $\text{Sr}_2\text{FeNbO}_6$  and  $\text{Sr}_2\text{FeTaO}_6$  are orthorhombic perovskites with a disordered distribution of cations over the six-coordinate sites [19,20]. At ~23 K they both undergo a transition to a spin-glass state; no long-range magnetic order was seen in a neutron diffraction experiment despite the fact that, when only nearest-neighbour interactions are considered, magnetic frustration is absent from the perovskite structure. This behaviour was explained by assuming that antiferromagnetic next-nearest-neighbour (NNN) interactions between  $\text{Fe}^{3+}$  cations, ~5.5 Å apart, were in competition with the nearest-neighbour interactions, thus introducing frustration. The NNN interactions take place along a  $90^\circ$  pathway of the form  $\text{Fe}-\text{O}-\text{M}-\text{O}-\text{Fe}$  and they will thus be stronger when  $\text{M}$  is a  $d^0$  cation, for example  $\text{Nb}^{5+}$  or  $\text{Ta}^{5+}$ , rather than a  $d^{10}$  cation, for example  $\text{Sn}^{4+}$ . This argument can be

extended to include  $\text{Ca}_2\text{CeCr}_2\text{TiO}_9$  wherein we propose that NNN interactions, mediated by  $\text{Ti}^{4+}$ , compete with NN Cr–O–Cr interactions. However, the relatively high concentration of  $\text{Cr}^{3+}$  cations ensures that in this case a G-type magnetic structure is established, although the competition from the NNN interactions ensures that, compared to  $\text{SrLaCrSnO}_6$ , a relatively small fraction,  $\sim 76\%$ , of the sites join the magnetic backbone.

## 5. Conclusion

The novel perovskites  $\text{SrLaCrSnO}_6$  and  $\text{Ca}_2\text{CeCr}_2\text{TiO}_9$  crystallise in the orthorhombic space group  $Pbnm$ . The magnetic properties of both can be explained by the formation of  $G_z$ -type antiferromagnetic clusters that grow in size upon cooling until they form a long-range-ordered magnetic backbone throughout the structure. Magnetic frustration, caused by competing superexchange interactions, can prevent all of the clusters coupling to the magnetic backbone even down to 2 K, causing hysteresis in magnetometry measurements and a low ordered moment per  $\text{Cr}^{3+}$  ion. The difference in the electronic structures of  $d^{10} \text{Sn}^{4+}$  and  $d^0 \text{Ti}^{4+}$  results in more of the magnetic clusters being decoupled from the magnetic backbone at low temperature in  $\text{Ca}_2\text{CeCr}_2\text{TiO}_9$  than in  $\text{SrLaCrSnO}_6$ .

## Acknowledgments

We thank the EPSRC for financial support under Grant EP/M018954/1 and Diamond Light Source Ltd (EE13284), ISIS Pulsed Neutron and Muon source and the Institut Laue-Langevin (ILL) for the award of beamtime. We also thank C. Murray for support on I11.

## Appendix A. Supporting information

Supplementary data associated with this article can be found in the online version at doi:10.1016/j.jssc.2018.10.037.

## References

- [1] M.T. Anderson, K.B. Greenwood, G.A. Taylor, K.R. Poeppelmeier, B-cation arrangements in double perovskites, *Prog. Solid State Chem.* 22 (1993) 197–233.
- [2] S. Vasala, M. Karppinen,  $A_2B'B''\text{O}_6$  perovskites: a review, *Prog. Solid State Chem.* 43 (2015) 1–36.
- [3] E.C. Hunter, P.D. Battle, R. Paria Sena, J. Hadermann, Ferrimagnetism as a consequence of cation ordering in the perovskite  $\text{LaSr}_2\text{Cr}_2\text{SbO}_9$ , *J. Solid State Chem.* 248 (2017) 96–103.
- [4] M. Retuerto, M. Garcia-Hernandez, M.J. Martinez-Lope, M.T. Fernandez-Diaz, J.P. Attfield, J.A. Alonso, Switching from ferro- to antiferromagnetism in  $\text{A}_2\text{CrSbO}_6$  ( $A = \text{Ca}, \text{Sr}$ ) double perovskites: a neutron diffraction study, *J. Mater. Chem.* 17 (2007) 3555–3561.
- [5] E.C. Hunter, P.D. Battle, Evolution of the crystal structure and magnetic properties of  $\text{Sr}_{2-x}\text{Ca}_x\text{CrSbO}_6$  with composition, *J. Solid State Chem.* 264 (2018) 48–58.
- [6] M.P. Attfield, P.D. Battle, S.K. Bollen, T.C. Gibb, R.J. Whitehead, The crystal structure and magnetic properties of  $\text{SrLaFeSnO}_6$  and  $\text{SrLaNiSbO}_6$ , *J. Solid State Chem.* 100 (1992) 37–48.
- [7] S.P. Thompson, J.E. Parker, J. Potter, T.P. Hill, A. Birt, T.M. Cobb, F. Yuan, C.C. Tang, Beamline I11 at Diamond: a new instrument for high resolution powder diffraction, *Rev. Sci. Instrum.* 80 (2009) 075107.
- [8] H.M. Rietveld, A profile refinement method for nuclear and magnetic structures, *J. Appl. Crystallogr.* 2 (1969) 65–71.
- [9] A.C. Larson, R.B. Von Dreele, Los Alamos Natl. Lab. Rep., LAUR, 1994, pp. 86–748.
- [10] Argonne National Laboratory Compute X-ray Absorption. (<http://11bm.xray.ap.s.anl.gov/absorb/absorb.php>).
- [11] W. David, Powder diffraction peak shapes. Parameterization of the pseudo-Voigt as a Voigt function, *J. Appl. Crystallogr.* 19 (1986) 63–64.
- [12] L.C. Chapon, P. Manuel, P.G. Radaelli, C. Benson, L. Perrott, S. Ansell, N.J. Rhodes, D. Raspino, D. Duxbury, E. Spill, J. Norris, Wish: the new powder and single crystal magnetic diffractometer on the second target station, *Neutron News* 22 (2011) 22–25.
- [13] E. Bertaut, Representation analysis of magnetic structures, *Acta Crystallogr. Sect. A* 24 (1968) 217–231.
- [14] R. Shannon, Revised effective ionic radii and systematic studies of interatomic distances in halides and chalcogenides, *Acta Crystallogr. Sect. A* 32 (1976) 751–767.
- [15] I. Qasim, P.E.R. Blanchard, S. Liu, B.J. Kennedy, M. Avdeev, Impact of Cu doping on the structure and electronic properties of  $\text{LaCr}_{1-y}\text{Cu}_y\text{O}_3$ , *Inorg. Chem.* 53 (2014) 2240–2247.
- [16] T.C. Gibb, Study of magnetic relaxation in the perovskite  $\text{SrLaFeSnO}_6$  by Mössbauer spectroscopy, *J. Mater. Chem.* 2 (1992) 415–422.
- [17] M. Tsegai, P. Nordblad, R. Tellgren, H. Rundlöf, G. André, F. Bourée, Synthesis, nuclear structure, and magnetic properties of  $\text{LaCr}_{1-y}\text{Mn}_y\text{O}_3$  ( $y = 0, 0.1, 0.2$ , and  $0.3$ ), *J. Alloy. Compd.* 457 (2008) 532–540.
- [18] O. Mustonen, S. Vasala, E. Sadrollahi, K.P. Schmidt, C. Baines, H.C. Walker, I. Terasaki, F.J. Litterst, E. Baggio-Saitovitch, M. Karppinen, Spin-liquid-like state in a spin-1/2 square-lattice antiferromagnet perovskite induced by  $d^{10}$ – $d^0$  cation mixing, *Nat. Commun.* 9 (1085) (2018).
- [19] N. Kashima, K. Inoue, T. Wada, Y. Yamaguchi, Low temperature neutron diffraction studies of  $\text{Sr}_2\text{FeMO}_6$  ( $M = \text{Nb}, \text{Sb}$ ), *Appl. Phys. A* 74 (2002) s805–s807.
- [20] P.D. Battle, T.C. Gibb, A.J. Herod, S.-H. Kim, P.H. Munns, Investigation of magnetic frustration in  $\text{A}_2\text{FeMO}_6$  ( $A = \text{Ca}, \text{Sr}, \text{Ba}$ ;  $M = \text{Nb}, \text{Ta}, \text{Sb}$ ) by magnetometry and Mössbauer spectroscopy, *J. Mater. Chem.* 5 (1995) 865–870.
- [21] K. Momma, F. Izumi, VESTA 3 for three-dimensional visualization of crystal, volumetric and morphology data, *J. Appl. Crystallogr.* 44 (2011) 1272–1276.